INTERNATIONAL JOURNAL FOR NUMERICAL METHODS IN FLUIDS, VOL. 11, 751–767 (1990)

UPWIND ADAPTIVE FINITE ELEMENT INVESTIGATIONS OF THE TWO-DIMENSIONAL REACTIVE INTERACTION OF SUPERSONIC GASEOUS JETS

D. CHARGY, A. DERVIEUX AND B. LARROUTUROU

INRIA. Sophia-Antipolis, 2004 Route des Lucioles F-06560 Valbonne, France

SUMMARY

We describe an upwind finite element method aimed at numerically simulating the two-dimensional transonic flow of a reactive gaseous mixture. The method uses in particular a triangular finite element mesh, with an adaptive procedure based on mesh refinement by triangle division, and an upwind non-oscillatory scheme based on an approximate Riemann solver for the evaluation of the convective terms for all species. Results concerning the reactive interaction of two supersonic gaseous jets are presented.

1. INTRODUCTION

Many industrial flows are so complex that the detailed understanding of the flow features is a very difficult task. In many of these situations the numerical simulation of these flows can play an essential role in this understanding and can allow one to better describe and explain the phenomena. This is especially true for engineering reactive flows. As a consequence, there is an increasing need for computer codes modelling the reactive flow of a gas mixture at various Mach numbers.

In these models the aerodynamic convective–acoustic effects often play an important role, which may cause difficulties for the stability of the numerical spatial approximation. These difficulties can be solved using a collection of tools: staggered grids, artificial viscosity methods, upwind schemes, high-resolution schemes of FCT (flux-corrected transport) or TVD (total variation diminishing) type (see e.g. Reference 1 and references therein for a review of most of these procedures). Furthermore, it is clear that the simulation of many of these complex phenomena requires an adequate adaptive gridding strategy: thus the design of performant numerical methods aimed at solving these complex problems should take into account both concerns of producing non-oscillatory results and allowing efficient mesh adaption.

One example of such complex physical phenomena requiring new numerical developments is the long-term objective of the work presented in this paper, which deals with the numerical simulation of the ignition process of a cryogenic rocket engine. During this process, cold two-phase gas/liquid propellant jets are ignited by interacting with a hot gaseous jet in the combustion chamber. This ignition process is certainly among the most complex engineering flow systems: it involves indeed three-dimensional effects, multi-phase flows, compressible effects (with, in particular, strong pressure ratios, supersonic regions and shock waves), turbulence, unsteadi-

0271–2091/90/140751–17$08.50

Received 6 November 1989

ness, a complete set of chemical reactions involving a large number of chemical species, high temperature and pressure ratios, etc.[2]

Because of the problem complexity, we will actually address in this study a simplified model problem: we will consider the ignition of a cold gaseous jet by a jet of hot gases, in a two-dimensional laminar inviscid flow, with a simplified one-step chemical mechanism, but with a detailed simulation of the flow, that is with an accurate resolution of the shock waves and of the combustion zone.

The numerical method used to solve this model problem uses an upwind non-oscillatory scheme constructed using multicomponent approximate Riemann solvers for the evaluation of the convective terms and a standard finite element formulation for the diffusive terms. This scheme operates on an unstructured finite element triangulation of the computational domain, which allows us to employ an adaptive mesh refinement procedure which locally divides the elements in order to improve the spatial resolution of the method in the thin reaction zone.

This numerical method is presented in the next section, while several numerical results are presented and discussed in Section 3.

2. NUMERICAL METHOD

2.1. The equations

As already said, we will concentrate on the simulation of multicomponent inviscid laminar gaseous flows. Our system of governing equations will therefore include the Euler equations, with additional continuity equations for each of the gaseous species and with additional diffusive and reactive terms in the energy and in the species equations. In fact, the viscous effects could be included without particular difficulty in our method,[3] which would essentially affect the numerical solution in the neighbourhood of the chamber walls.

In order to present the numerical method, we simply consider for the moment a mixture made of two species Σ_1 and Σ_2, whose mass fractions will be denoted by Y_1 and Y_2 (that is, ρY_1 and ρY_2 are the separate densities of the two species, ρ being the mixture density). Since $Y_2 = 1 - Y_1$, we will often consider only Y_1 and simply set $Y_1 = Y$.

The two-dimensional reactive flow of this two-component mixture is described by the following system of governing equations:[4,5]

$$
\begin{aligned}
&\rho_t + (\rho u)_x + (\rho v)_y = 0,\\
&(\rho u)_t + (\rho u^2 + p)_x + (\rho uv)_y = 0,\\
&(\rho v)_t + (\rho uv)_x + (\rho v^2 + p)_y = 0,\\
&E_t + [u(E+p)]_x + [v(E+p)]_y = \nabla\cdot(\lambda \nabla T) + \Omega_T + \sum_{k=1}^{2} \nabla\cdot(\rho D C_{pk} T \nabla Y_k),\\
&(\rho Y)_t + (\rho u Y)_x + (\rho v Y)_y = \nabla\cdot(\rho D \nabla Y) + \Omega_Y,
\end{aligned}
\tag{1}
$$

$$
E = \sum_{k=1}^{2} \rho Y_k C_{vk} T + \tfrac{1}{2}\rho(u^2 + v^2),
$$

$$
p = \sum_{k=1}^{2} \frac{\rho Y_k R T}{M_k}. \tag{2}
$$

Our notations are classical: u and v are the components of the mixture velocity $\mathbf{U}$, p is the pressure, E is the sum of the internal and kinetic energies per unit volume, λ is the mixture thermal

conductivity, T is the temperature and D is the molecular diffusion coefficient of species Σ_1. We have assumed that both species behave as perfect gases but that Σ_1 and Σ_2 may have different specific heats C_{v1}, C_{v2}, C_{p1} and C_{p2} and different molecular weights M_1 and M_2. Lastly, the source terms Ω_T and Ω_Y represent the contribution of the chemical reactions to the energy and mass fraction equations (these terms will be made precise later for the specific problem considered in our calculations). We will assume below that the quantities λ, ρD, C_{pk} and C_{vk} are constant.

2.2. *Spatial approximation*

We now present the numerical scheme used to solve equations (1), (2); this scheme is a mixed finite element/finite volume scheme. More precisely, it uses for the hyperbolic terms appearing in the left-hand side of system (1) an upwind formulation which is derived by extending to mixtures some of the usual approximate Riemann solvers used to solve the Euler equations of a single inviscid gas.[6] Moreover, it operates on an unstructured finite element triangulation, which makes it possible to employ a computational mesh fitted to complex geometries and adapted to complex solutions (involving, for instance, strong shocks or thin flames). This scheme can be extended to three-dimensional calculations in a straightforward way (see e.g. Reference 7).

To specify the scheme, we first rewrite system (1), (2) in the following form:

$$\mathbf{W}_t+\mathbf{F}(\mathbf{W})_x+\mathbf{G}(\mathbf{W})_y=\mathbf{P}(\mathbf{W})_x+\mathbf{Q}(\mathbf{W})_y+\mathbf{S}(\mathbf{W}),$$

$$\mathbf{W}=\begin{bmatrix}\rho\\ \rho u\\ \rho v\\ E\\ \rho Y\end{bmatrix},\qquad \mathbf{F}(\mathbf{W})=\begin{bmatrix}\rho u\\ \rho u^2+p\\ \rho uv\\ u(E+p)\\ \rho uY\end{bmatrix},\qquad \mathbf{G}(\mathbf{W})=\begin{bmatrix}\rho u\\ \rho uv\\ \rho v^2+p\\ v(E+p)\\ \rho vY\end{bmatrix},$$

$$\mathbf{P}(\mathbf{W})=\begin{bmatrix}0\\ 0\\ 0\\ \lambda T_x+\sum_{k=1}^{2}\rho DC_{pk}T(Y_k)_x\\ \rho DY_x\end{bmatrix},\qquad \mathbf{Q}(\mathbf{W})=\begin{bmatrix}0\\ 0\\ 0\\ \lambda T_y+\sum_{k=1}^{2}\rho DC_{pk}T(Y_k)_y\\ \rho DY_y\end{bmatrix},$$

$$\mathbf{S}(\mathbf{W})=\begin{bmatrix}0\\ 0\\ 0\\ \Omega_T\\ \Omega_Y\end{bmatrix}. \tag{3}$$

Then we introduce a finite element triangulation of the computational domain. In order to derive a finite volume formulation, we consider a dual partition of the domain in control volumes or cells: a cell C_i is constructed around each vertex S_i by means of the medians of the neighbouring triangles, as shown in Figure 1.

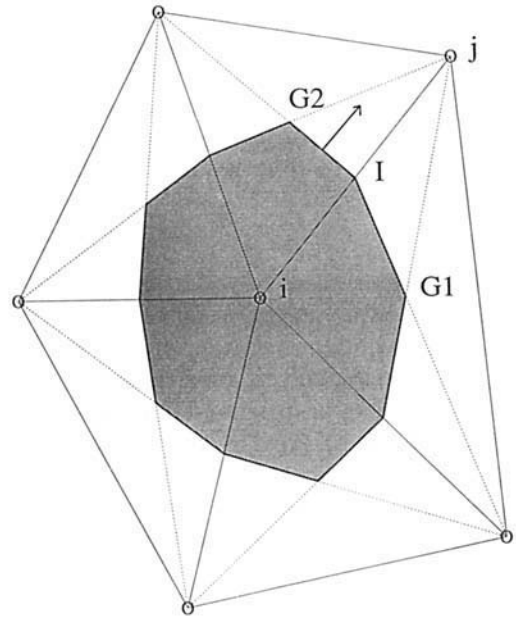

Figure 1. Control volume C_i around vertex S_i

Integrating system (3) on the control volume C_i, we get

$$\iint_{C_i} \mathbf{W}_t + \int_{\partial C_i} (\mathbf{F} v_i^x + \mathbf{G} v_i^y) = \int_{\partial C_i} (\mathbf{P} v_i^x + \mathbf{Q} v_i^y) + \iint_{C_i} \mathbf{S}(\mathbf{W}), \tag{4}$$

where $\nu = (v_i^x, v_i^y)$ is the outward unit normal on ∂C_i. It now remains to specify how the four integrals in (4) are evaluated.

The time derivative and source terms integrals are approximated using a mass-lumped approximation:

$$\iint_{C_i} \mathbf{W}_t = \frac{\mathrm{d}\mathbf{W}_i}{\mathrm{d}t} \mathrm{area}(C_i), \qquad \iint_{C_i} \mathbf{S}(\mathbf{W}) = \mathbf{S}(\mathbf{W}_i) \mathrm{area}(C_i). \tag{5}$$

In addition to its simplicity, the mass-lumped approximation has two advantages: first, it allows us to employ an explicit time integration scheme, which is no longer possible when the consistent non-diagonal mass matrix is used; moreover, the mass-lumped approximation of the heat equation conserves the positiveness of the unknowns, while a consistent finite element formulation does not.

To approximate the second integral in (4), we begin by noticing that (2) yields (using Mayer's relation $M_k(C_{pk} - C_{vk}) = R$)

$$p = (\gamma - 1)[E - \tfrac{1}{2}\rho(u^2 + v^2)], \tag{6}$$

where γ is the local specific heat ratio of the mixture:

$$\gamma = \frac{\sum_{k=1}^{2} Y_k C_{pk}}{\sum_{k=1}^{2} Y_k C_{vk}}. \tag{7}$$

It is now a well known fact that the system

$$\mathbf{W}_t + \mathbf{F}(\mathbf{W})_x + \mathbf{G}(\mathbf{W})_y = 0, \tag{8}$$

with the pressure p given by (6), (7), is a non-linear *hyperbolic* system of conservation laws.[8-10] For any $(\alpha, \beta) \in \mathbb{R}^2$, the matrix $\alpha \partial \mathbf{F}/\partial \mathbf{W} + \beta \partial \mathbf{G}/\partial \mathbf{W}$ has five real eigenvalues:

$$\begin{aligned} \lambda_1 &= \alpha u + \beta v - \sqrt{(\alpha^2 + \beta^2)}c, \\ \lambda_2 &= \lambda_3 = \lambda_4 = \alpha u + \beta v, \\ \lambda_5 &= \alpha u + \beta v + \sqrt{(\alpha^2 + \beta^2)}c, \end{aligned} \tag{9}$$

with $c = \sqrt{(\gamma p/\rho)}$, and a complete set of real eigenvectors.

Using this fact, we define an 'approximate Riemann solver' for system (6)–(8). We use here an extension to mixtures of Roe's scheme[11] (we refer to References 8–10 for more details on the extension of the classical Godunov-type schemes and flux vector splittings to system (6)–(8)). Given two values $\mathbf{W}_L$ and $\mathbf{W}_R$ of $\mathbf{W}$, and a vector $\boldsymbol{\eta} = (\eta^x, \eta^y)$, we define a numerical flux function $\boldsymbol{\Phi}$ by:

$$\boldsymbol{\Phi}(\mathbf{W}_L, \mathbf{W}_R, \boldsymbol{\eta}) = \tfrac{1}{2}[\mathscr{F}_\eta(\mathbf{W}_L) + \mathscr{F}_\eta(\mathbf{W}_R)] + \tfrac{1}{2}|\tilde{\mathbf{H}}_\eta|(\mathbf{W}_R - \mathbf{W}_L). \tag{10}$$

In this expression we have set $\mathscr{F}_\eta(\mathbf{W}) = \eta^x \mathbf{F}(\mathbf{W}) + \eta^y \mathbf{G}(\mathbf{W})$, and $\tilde{\mathbf{H}}_\eta = \tilde{\mathbf{H}}_\eta(\mathbf{W}_L, \mathbf{W}_R)$ is a diagonalizable matrix satisfying Roe's property:

$$\mathscr{F}_\eta(\mathbf{W}_L) - \mathscr{F}_\eta(\mathbf{W}_R) = \tilde{\mathbf{H}}_\eta(\mathbf{W}_L, \mathbf{W}_R)(\mathbf{W}_R - \mathbf{W}_L). \tag{11}$$

The matrix $|\tilde{\mathbf{H}}_\eta|$ is defined using the diagonalization of $\tilde{\mathbf{H}}_\eta$: if $\tilde{\mathbf{H}} = \mathbf{T}\tilde{\boldsymbol{\Lambda}}\mathbf{T}^{-1}$ with $\tilde{\boldsymbol{\Lambda}}$ diagonal, $\tilde{\boldsymbol{\Lambda}} = (\tilde{\lambda}_k)_{k=1,5}$, then we set

$$|\tilde{\mathbf{H}}| = \mathbf{T}|\tilde{\boldsymbol{\Lambda}}|\mathbf{T}^{-1}, \quad \text{with} \quad |\tilde{\boldsymbol{\Lambda}}| = (|\tilde{\lambda}_k|)_{k=1,5}. \tag{12}$$

To evaluate the second integral in (4), we first write it in the form

$$\int_{\partial C_i} (\mathbf{F} v_i^x + \mathbf{G} v_i^y) = \sum_{j \in \mathscr{K}(i)} \int_{\partial C_{ij}} (\mathbf{F} v_i^x + \mathbf{G} v_i^y), \tag{13}$$

where $\mathscr{K}(i)$ is the set of neighbouring nodes of S_i and where $\partial C_{ij} = \partial C_i \cap \partial C_j$. Then, defining the vector $v_{ij} = (v_{ij}^x, v_{ij}^y)$ by

$$v_{ij}^x = \int_{\partial C_{ij}} v_i^x, \qquad v_{ij}^y = \int_{\partial C_{ij}} v_i^y, \tag{14}$$

we obtain a first-order accurate upwind approximation of the convective flux (13) by

$$\int_{\partial C_i} (\mathbf{F} v_i^x + \mathbf{G} v_i^y) = \sum_{j \in \mathscr{K}(i)} \boldsymbol{\Phi}(\mathbf{W}_i, \mathbf{W}_j, v_{ij}). \tag{15}$$

A second-order accurate upwind extension can be derived by using a MUSCL-type approximation instead of a constant-by-cell approximation. In this case (15) becomes

$$\int_{\partial C_i} (\mathbf{F} v_i^x + \mathbf{G} v_i^y) = \sum_{j \in \mathscr{K}(i)} \boldsymbol{\Phi}(\mathbf{W}_{ij}, \mathbf{W}_{ji}, v_{ij}), \tag{16}$$

where the same numerical flux function $\boldsymbol{\Phi}$ is used, but where $\mathbf{W}_{ij}$ (resp. $\mathbf{W}_{ji}$) is a second-order accurate approximation of $\mathbf{W}$ at the cell interface ∂C_{ij} inside the cell C_i (resp. inside the cell C_j). To construct these values $\mathbf{W}_{ij}$ and $\mathbf{W}_{ji}$, we first define an approximate gradient of $\mathbf{W}$ at the vertex

S_i by the formulae

$$\mathbf{W}_x(i) = \frac{1}{\text{area}[\mathscr{T}(i)]} \iint_{\mathscr{T}(i)} \frac{\partial \mathbf{W}}{\partial x} \, dx \, dy,$$

$$\mathbf{W}_y(i) = \frac{1}{\text{area}[\mathscr{T}(i)]} \iint_{\mathscr{T}(i)} \frac{\partial \mathbf{W}}{\partial y} \, dx \, dy, \tag{17}$$

where $\mathscr{T}(i)$ denotes the union of those triangles which have S_i as a vertex, and where the integrands $\partial \mathbf{W}/\partial x$ and $\partial \mathbf{W}/\partial y$ are the derivatives of the usual P1 Galerkin interpolant of $\mathbf{W}$. We can then evaluate $\mathbf{W}_{ij}$ and $\mathbf{W}_{ji}$ as

$$\mathbf{W}_{ij} = \mathbf{W}_i + \tfrac{1}{2} \nabla \mathbf{W}(i) \cdot \mathbf{S}_i \mathbf{S}_j,$$

$$\mathbf{W}_{ji} = \mathbf{W}_j + \tfrac{1}{2} \nabla \mathbf{W}(j) \cdot \mathbf{S}_j \mathbf{S}_i. \tag{18}$$

In fact, the fully second-order accurate approximation defined by (16)–(18) may produce oscillatory results and thus is not employed in this form; we use instead a TVD-like scheme derived by using 'limited' extrapolated values $\mathbf{W}^l_{ij}$ and $\mathbf{W}^l_{ji}$ in place of $\mathbf{W}_{ij}$ and $\mathbf{W}_{ji}$ in (16). We refer to Reference 12 for the details.

Lastly, we consider the integral of the diffusive fluxes, $\int_{\partial C_i} (\mathbf{P} v_i^x + \mathbf{Q} v_i^y)$. In view of the definitions (3) of $\mathbf{P}$ and $\mathbf{Q}$, this integral reduces to expressions like

$$\int_{\partial C_i} \nabla T \cdot \boldsymbol{\nu}_i, \quad \int_{\partial C_i} \nabla Y \cdot \boldsymbol{\nu}_i \quad \text{and} \quad \int_{\partial C_i} T \nabla Y \cdot \nu_i. \tag{19}$$

To evaluate these terms, we consider here that the integrands are constant in each triangle τ of the triangulation. More precisely, we consider that, in a triangle τ with vertices $S_j (1 \leqslant j \leqslant 3)$, we have

$$\nabla \mathbf{T}|_\tau = \sum_{j=1}^{3} T_j \nabla \phi_j, \qquad \nabla Y|_\tau = \sum_{j=1}^{3} Y_j \nabla \phi_j, \tag{20}$$

where ϕ_j is the P1 finite element basis function associated to vertex S_j and, for the last term in (19),

$$T|_\tau = \tfrac{1}{3} \sum_{j=1}^{3} T_j. \tag{21}$$

Then the diffusive term in (4) takes the value

$$\int_{\partial C_i} (\mathbf{P} v_i^x + \mathbf{Q} v_i^y) = \sum_{\tau \in \mathscr{T}(i)} \begin{pmatrix} \mathbf{P}_\tau \\ \mathbf{Q}_\tau \end{pmatrix} \int_{\partial C_i \cap \tau} \nu_i, \tag{22}$$

where $\mathbf{P}_\tau$ and $\mathbf{Q}_\tau$ are the constant values of $\mathbf{P}$ and $\mathbf{Q}$ in the triangle τ. It is easy to check that (20)–(22) are equivalent to a classical finite element discretization of the diffusive terms.

2.3. Boundary conditions

Let Γ be the boundary of the computational domain and $\mathbf{n}$ be the outward unit normal on Γ. We assume that Γ is divided into two parts, $\Gamma = \Gamma_0 \cup \Gamma_\infty$, on which different boundary conditions will be used. In this partition, Γ_0 represents a solid wall while Γ_∞ represents the far-field (inflow or outflow) boundaries.

In our scheme we do not treat a boundary condition by forcing the value of a variable to a prescribed boundary value, but consider instead the integral formulation (4) and apply the

boundary conditions by modifying the flux integrals on ∂C_i for those cells C_i such that $\partial C_i \cap \Gamma \neq \varnothing$.

For instance, for a vertex S_i located on Γ_0 we do not impose the slip condition $\mathbf{U} \cdot \mathbf{n} = 0$ but take this condition into account in the evaluation of the convective fluxes, getting

$$\int_{\partial C_i \cap \Gamma_0} \mathbf{F} n^x + \mathbf{G} n^y = \begin{bmatrix} 0 \\ \int_{\partial C_i \cap \Gamma_0} p n^x \\ \int_{\partial C_i \cap \Gamma_0} p n^y \\ 0 \\ 0 \end{bmatrix}; \tag{23}$$

the pressure integrals are computed as

$$\int_{\partial C_i \cap \Gamma_0} p n^x = p_i \int_{\partial C_i \cap \Gamma_0} n^x, \qquad \int_{\partial C_i \cap \Gamma_0} p n^y = p_i \int_{\partial C_i \cap \Gamma_0} n^y. \tag{24}$$

Moreover, assuming that the wall is adiabatic and non-catalytic ($\nabla T = 0$ and $\nabla Y = 0$ on Γ_0), we set

$$\int_{\partial C_i \cap \Gamma_0} \mathbf{P} n^x + \mathbf{Q} n^y = 0. \tag{25}$$

For a vertex S_i located on Γ_∞ we again set

$$\int_{\partial C_i \cap \Gamma_\infty} \mathbf{P} n^x + \mathbf{Q} n^y = 0, \tag{26}$$

which amounts to assuming that the temperature and mass fraction gradients vanish at the far-field boundary Γ_∞. To evaluate the convective fluxes on $\partial C_i \cap \Gamma_\infty$, we again use an approximate Riemann solver: the difficulty here is that, in the problems we consider below, the flow may be subsonic on some part of Γ_∞ and supersonic on other parts of this boundary. More precisely, we define a 'far-field solution' $\mathbf{W}_\infty$, we define $\mathbf{n}_i = \int_{\partial C_i \cap \Gamma_\infty} \mathbf{n}$ and we set, in agreement with (15),

$$\int_{\partial C_i \cap \Gamma_\infty} (\mathbf{F} n^x + \mathbf{G} n^y) = \hat{\mathbf{\Phi}}(\mathbf{W}_i, \mathbf{W}_\infty, \mathbf{n}_i), \tag{27}$$

where $\hat{\mathbf{\Phi}}$ is again a numerical flux function. Here we use for simplicity a flux function $\hat{\mathbf{\Phi}}$ 'of the Steger–Warming type'[13] instead of Roe's flux function (10), namely

$$\hat{\mathbf{\Phi}}(\mathbf{W}_i, \mathbf{W}_\infty, \eta) = \mathbf{H}_\eta^+(\mathbf{W}_i)\mathbf{W}_i + \mathbf{H}_\eta^-(\mathbf{W}_i)\mathbf{W}_\infty; \tag{28}$$

in this expression, $\mathbf{H}_\eta$ is the Jacobian matrix $\partial \mathscr{F}_\eta / \partial \mathbf{W}$ and $\mathbf{H}_\eta^+$, $\mathbf{H}_\eta^-$ are defined in the classical way: if $\mathbf{H} = \mathbf{T}\mathbf{\Lambda}\mathbf{T}^{-1}$ with $\mathbf{\Lambda}$ diagonal, $\mathbf{\Lambda} = (\lambda_k)_{k=1,5}$, then $\mathbf{H}^\pm = \mathbf{T}\mathbf{\Lambda}^\pm\mathbf{T}^{-1}$ with $\mathbf{\Lambda}^\pm = (\lambda_k^\pm)_{k=1,5}$.

In fact, for reasons which will appear in the next subsection, we will use instead of (28) the following more general flux:

$$\hat{\mathbf{\Phi}}_\beta(\mathbf{W}_i, \mathbf{W}_\infty, \eta) = \mathbf{H}_\eta^+(\mathbf{W}_i)\mathbf{W}_i + \mathbf{H}_\eta^-(\mathbf{W}_i)[\beta \mathbf{W}_i + (1-\beta)\mathbf{W}_\infty], \tag{29}$$

where β is a positive parameter to be adequately chosen (see Section 3.2 below).

2.4. Time integration

Because the objective of our study is to simulate the unsteady ignition process, we do not attempt to use large time steps but simply use the classical first-order accurate forward Euler scheme to advance in time the numerical solution.

We then have a stability restriction on the time step. The analysis of the stability of the whole non-linear scheme being too complex, we derive three approximate stability conditions by considering separately the hyperbolic terms, the diffusive terms and the reactive terms. By considering only the hyperbolic terms ($\mathbf{W}_t + \mathbf{F}_x + \mathbf{G}_y = 0$), we obtain the convective–acoustic stability condition:

$$\frac{\Delta t}{\Delta h} \max(|U + c|, |U|, |U - c|) \leqslant 1 \tag{30}$$

(Δh is a measure of the mesh spacing). By considering the diffusive terms only

$$(E_t = \lambda \Delta T = \lambda \Delta [E/\rho \textstyle\sum_{k=1}^{2} Y_k C_{vk} - \frac{1}{2}(u^2 + v^2)] \quad \text{and} \quad (\rho Y)_t = \Delta(\rho D Y)),$$

we obtain the diffusive stability condition

$$\frac{2\Delta t}{\Delta h^2} \max\left(\frac{\lambda}{\rho \sum_{k=1}^{2} Y_k C_{vk}}, D\right) \leqslant 1. \tag{31}$$

Lastly, by considering only the reactive terms, we obtain a reactive stability condition (in short, this condition says that the time step may not be greater than the smallest characteristic time scale of the chemical reactions occuring in the mixture; we cannot write this condition down until we have specified these reactions).

3. NUMERICAL RESULTS

To show how the above described numerical scheme performs when applied to the jet interaction problem mentioned in the introduction, we will now consider in sequence two numerical experiments with two different geometries.

3.1. Results with two species

In a first step we consider only two gaseous species, $\sum_1$ and $\sum_2$, which have the same specific heats and molecular weight. In the geometry of Figure 1, a cold jet of species $\sum_1$ is injected through the top orifice of the chamber and a hot jet of species $\sum_2$ is injected through the left orifice. The Mach number and the non-dimensionalized pressure and temperature of the two jets at injection are the following:

$$\begin{aligned} &\mathcal{M}_1 = 1{\cdot}7, \quad p_1 = 810, \quad T_1 = 3{\cdot}54, \\ &\mathcal{M}_2 = 1{\cdot}1, \quad p_2 = 11700, \quad T_2 = 15{\cdot}7. \end{aligned} \tag{32}$$

As initial conditions we use a uniform field $\mathbf{W}_0$ defined by

$$u_0 = v_0 = 0, \quad p_0 = 500, \quad T_0 = 5{\cdot}5, \quad (Y_1)_0 = 0, \quad (Y_2)_0 = 1. \tag{33}$$

In Figure 2 the dotted part of the boundary represents 'far-field' (inflow or outflow)' boundaries. The uniform field $\mathbf{W}_0$ is used as the far-field solution at the outflow boundary (i.e. $\mathbf{W}_\infty = \mathbf{W}_0$). The triangulation is uniform, with 3322 nodes.

Figures 2 and 3 show the Mach contours at two successive time levels for a purely aerodynamical calculation (no diffusive effects: $\lambda = 0$, $D = 0$; and no reaction: $\Omega_T = 0$, $\Omega_Y = 0$). The barrel shock and the Mach disk clearly appear at the intermediate time level of Figure 2. In the steady state of Figure 3 one can observe the large deviation of the cold jet, which is expected since the cold jet momentum is rather small compared with the hot jet momentum.

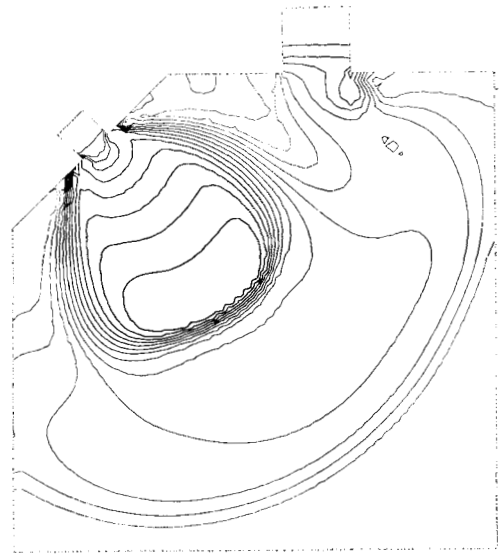

Figure 2. Mach contours at an intermediate time (without combustion)

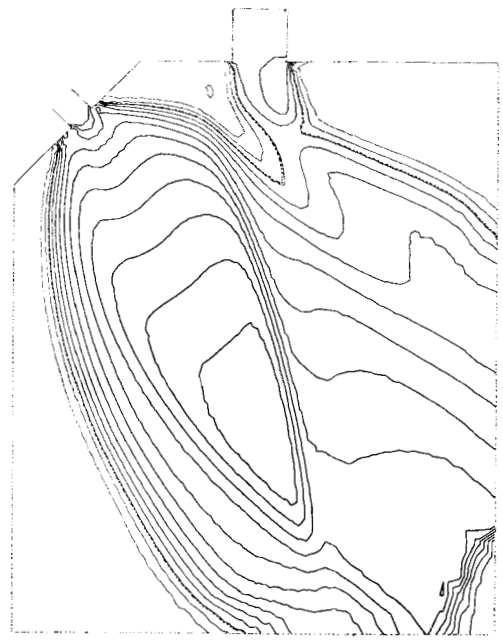

Figure 3. Steady state Mach contours (without combustion)

All these results have been computed with the boundary flux (28), i.e. with $\beta = 0$ in (29). Some difficulties with the treatment of the boundary conditions appear at the bottom right corner of Figure 3, where a shock wave remains "trapped' inside the computational domain. These difficulties are of course due to the facts that we use a far-field solution $\mathbf{W}_\infty$ which is constant along the boundary Γ_∞ and that the outflow boundary is not far enough from the injectors. This is the reason why we will use the modified β-flux (29) (see Section 3.2. below).

With the same geometry and injection conditions, we now consider the diffusive and reactive effects described in system (1). More precisely, we assume that the simple one-step reaction $\sum_1 \rightarrow \sum_2$ occurs in the mixture; thus the reaction terms in (1) take the form

$$\Omega_T = Q\omega, \qquad \Omega_Y = -M_1\omega, \qquad \omega = \rho Y \exp\left(-\frac{\mathscr{E}}{RT}\right), \tag{34}$$

where Q is the heat released by the reaction and $\mathscr{E}$ is the activation energy of the reaction.

As expected from the physical point of view, a flame develops in the region where the cold jet of reactant is heated by the hot jet of products (see Figures 4 and 5, where the problem at the bottom right corner again appears).

We have also studied a similar experience in a simpler rectangular geometry. The injection conditions are the same as in (32), except that we have decreased the cold jet temperature to $T_1 = 2$ in order to increase the temperature ratio between the two jets. Figures 6 and 7 allows to compare the steady flames obtained on a uniform mesh with 357 nodes and on a locally refined adaptive mesh with 1026 nodes. The refined mesh, which is shown on Figure 8, is constructed by using the following strategy twice: any triangle in which the reaction rate ω (computed on the coarse uniform mesh) is larger than a given value is divided into four new triangles; then each triangle in the first row of undivided triangles is also divided into two or three subtriangles in order to obtain

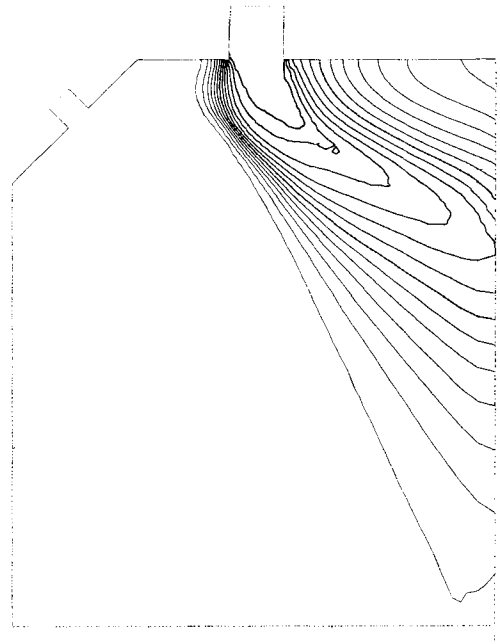

Figure 4. Mass fraction contours (with combustion)

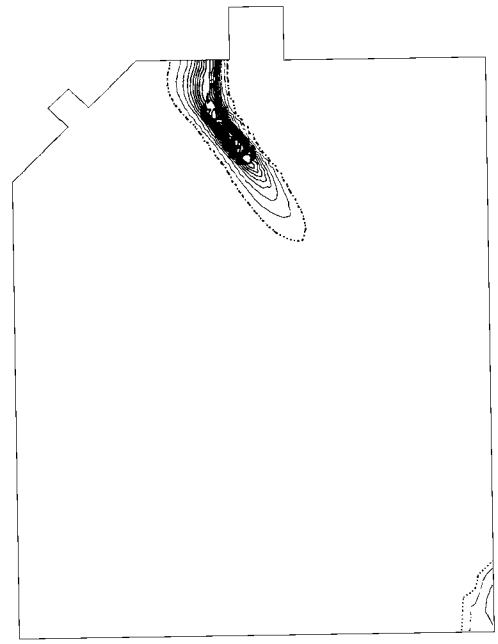

Figure 5. Reaction rate contours

an admissible finite element triangulation (see Reference 14 for more details). The improvement in the accuracy of the flame simulation appears very clearly in Figures 6 and 7.

3.2. Three-species calculations

In order to consider a problem which is closer to the actual ignition process of a rocket engine, we now assume that the molecular weight of the hot gases (injected on the left) is much higher than the molecular weight of the cold jet of reactant, which will allow us to increase the temperature ratio between the two jets while respecting the Mach number and pressure ratios given by (32). More precisely, we will consider that the mixture is made of three species: the species $\sum_1$ injected in the cold jet is able to react according to the reaction $\sum_1 \rightarrow \sum_2$ ($\sum_1$ and $\sum_2$ having the same specific heats and molecular weights), and the hot jet is made of species $\sum_3$, with $M_3 > M_1$.

Compared to the results obtained with two species, the situation appears to be more complicated when three species are considered, and new phenomena appear. Figures 9–12 show the steady state mass fraction contours for species $\sum_1$ and $\sum_3$ and the steady Mach contours for a purely aerodynamical calculation. In particular, Figures 11 and 12 show how the use of the β-flux (29) at the outflow boundary improves the quality of the numerical results (the value $\beta = 0{\cdot}8$ has been chosen on the basis on some simplified analysis of the resulting scheme; see Reference 15 for more details). Figures 13–15 correspond to a (non-steady) situation with combustion, where it appears that the influence of the flame on the aerodynamical field is much more important than in the two-species calculation.

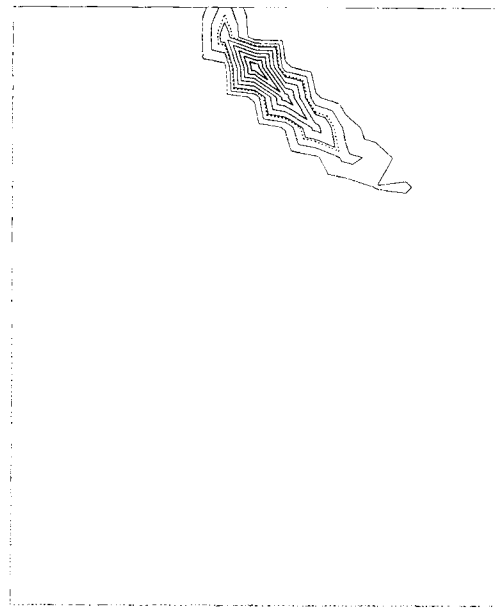

Figure 6. Reaction rate contours on a coarse mesh (simplified geometry)

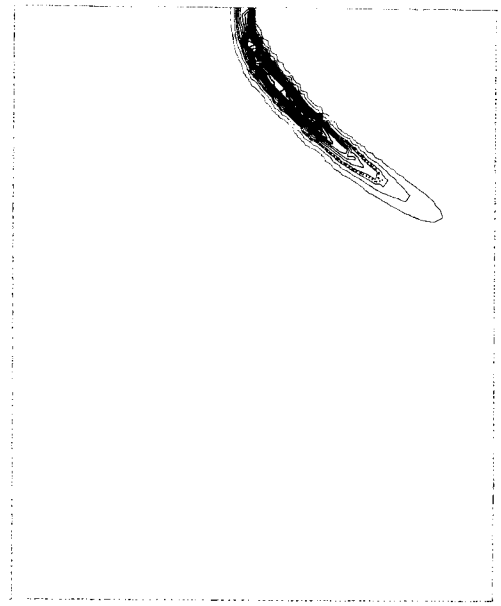

Figure 7. Reaction rate contours on a refined mesh (simplified geometry)

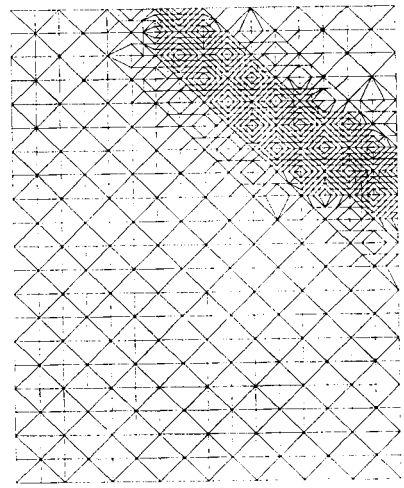

Figure 8. Refined mesh

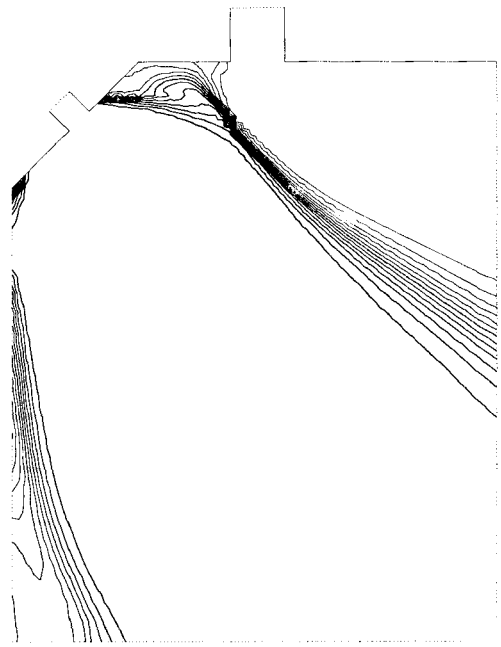

Figure 9. Mass fraction contours of the third species (without combustion, $\beta=0{\cdot}8$)

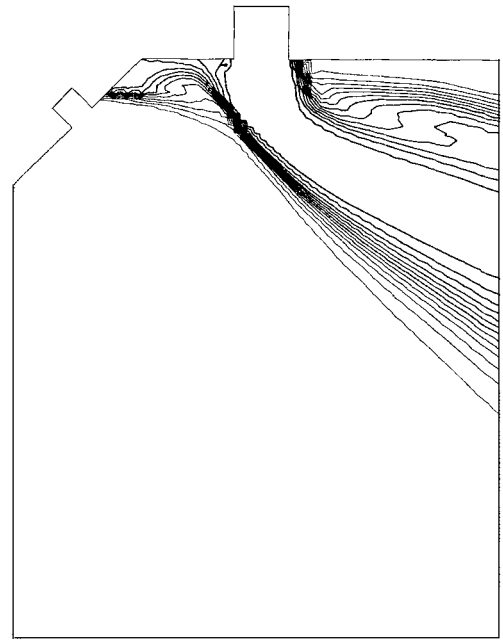

Figure 10. Mass fraction contours of the first species (without combustion, $\beta = 0{\cdot}8$)

Figure 11. Mach contours (without combustion, $\beta = 0{\cdot}8$)

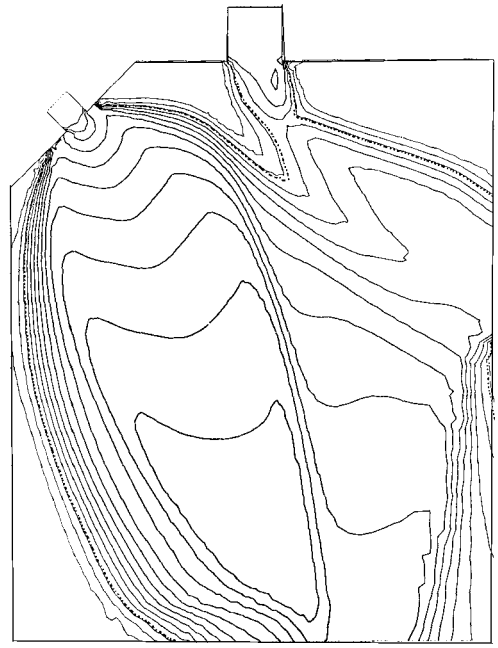

Figure 12. Mach contours (without combustion, $\beta = 0$)

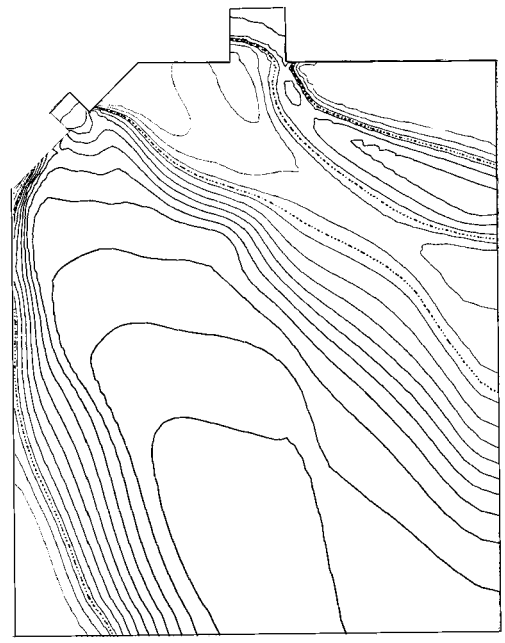

Figure 13. Mach contours (with combustion, $\beta = 0{\cdot}8$)

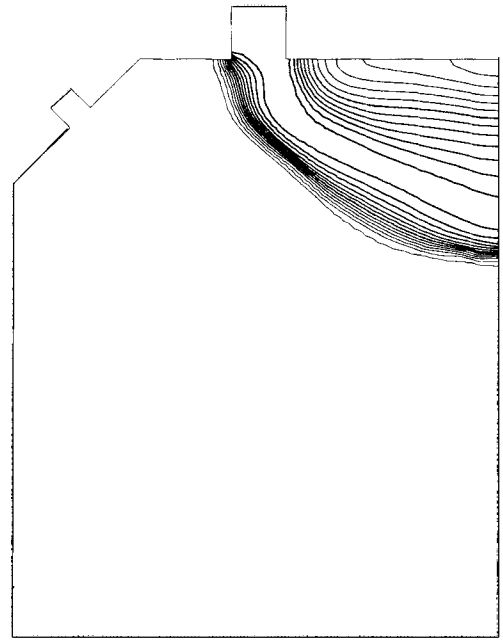

Figure 14. Mass fraction contours of the first species (with combustion, $\beta = 0{\cdot}8$)

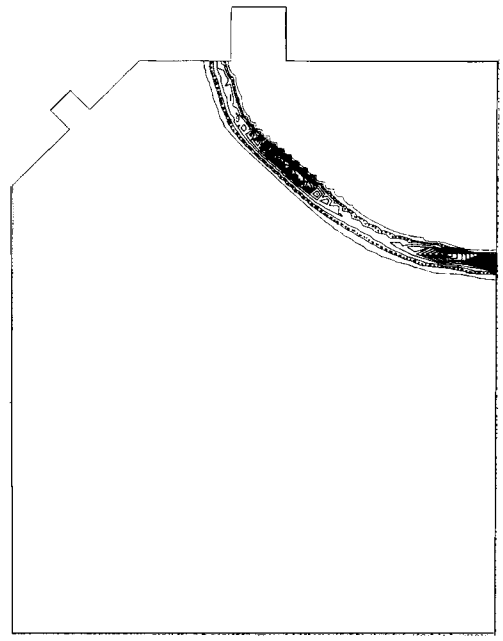

Figure 15. Reaction rate contours ($\beta = 0{\cdot}8$)

REFERENCES

1. V. Selmin, 'Finite-element solution of hyperbolic equations—I: One-dimensional case', *INRIA Report 655*, 1987.
2. P. Liang, S. Fisher and Y. M. Chang, 'Comprehensive modeling of a liquid rocket combustion chamber', *AIAA Paper 85-0232*, 1985.
3. F. Fezoui, S. Lanteri, B. Larrouturou and C. Olivier, 'Résolution numérique des équations de Navier Stokes pour un fluide compressible en maillage triangulaire', *INRIA Report 1033*, 1989.
4. J. D. Buckmaster and G. S. S. Ludford, *Theory of Laminar Flames*, Cambridge University Press, Cambridge, 1982.
5. F. A. Williams, *Combustion Theory*, 2nd edn, Benjamin Cummings, Menlo Park, 1985.
6. A. Harten, P. D. Lax and B. Van Leer, 'On upstream differencing and Godunov type schemes for hyperbolic conservation laws', *SIAM Rev.*, **25**, 35–61 (1983).
7. B. Stoufflet, J. Periaux, F. Fezoui and A. Dervieux, 'Numerical simulation of 3-D hypersonic Euler flow around space vehicle using adapted finite elements', *AIAA Paper 87-0560*, 1987.
8. R. Abgrall, 'Généralisation du schéma de Roe pour le calcul d'écoulements de mélanges de gaz à concentrations variables', *La Recherche Aérospatiale*, **6**, 31–43 (1988).
9. G. Fernandez and B. Larrouturou, 'Hyperbolic schemes for multicomponent Euler equations', in J. Ballmann and R. Jeltsch (eds.), *Nonlinear Hyperbolic Equations—Theory, Numerical Methods and Applications*; *Notes on Numerical Fluid Mechanics, Vol. 24*, Vieweg, Braunschweig, 1989, pp. 128–138.
10. B. Larrouturou and L. Fezoui, 'On the equations of multi-component perfect or real gas inviscid flow', in C. Carasso, P. Charrier, B. Hanouzet and J. L. Joly (eds.), *Nonlinear Hyperbolic Problems*; *Lecture Notes in Mathematics, Vol. 1402*, Springer, Heidelberg, 1989, pp. 69–98.
11. P. L. Roe, 'Approximate Riemann solvers, Parameter vectors and difference schemes' *J. Comput. Phys.*, **43**, 357 (1981).
12. F. Fezoui, 'Résolution des équations d'Euler par un schéma de Van Leer en éléments finis' *INRIA Report 358*, 1985.
13. J. L. Steger and R. F. Warming, 'Flux vector splitting for the inviscid gas dynamic equations with applications to finite-difference methods' *J. Comput. Phys.*, **40**, 263–293 (1981).
14. B. Palmerio, 'Self adaptive FEM algorithms for the Euler equations', *INRIA Report 338*, 1984.
15. D. Chargy, 'Simulation numérique d'écoulements réactifs transsoniques', *Thesis*, to appear.